A new insight of the vertical differences of NO₂ heterogeneous reaction to produce HONO over inland and marginal seas

Chengzhi Xing[a], Shiqi Xu[g], Cheng Liu[b,a,c,d,*], Yuhan Liu[f], Keding Lu[e,*], Wei Tan[a], Qihou Hu[a], Shanshan Wang[i], Hongyu Wu[h], and Hua Lin[h]

[a] Key Lab of Environmental Optics & Technology, Anhui Institute of Optics and Fine Mechanics, Hefei Institutes of Physical Science, Chinese Academy of Sciences, Hefei 230031, China

[b] Department of Precision Machinery and Precision Instrumentation, University of Science and Technology of China, Hefei, 230026, China

[c] Center for Excellence in Regional Atmospheric Environment, Institute of Urban Environment, Chinese Academy of Sciences, Xiamen, 361021, China

[d] Key Laboratory of Precision Scientific Instrumentation of Anhui Higher Education Institutes, University of Science and Technology of China, Hefei, 230026, China

[e] State Key Joint Laboratory of Environment Simulation and Pollution Control, College of Environmental Sciences and Engineering, Peking University, Beijing 100871, China

[f] Department of unclear safety, Chia Institute of Atomic Energy, Beijing, 102413, China

[g] School of Earth and Space Sciences, University of Science and Technology of China, Hefei, 230026, China.

[h] School of Environmental Science and Optoelectronic Technology, University of Science and Technology of China, Hefei, 230026, China

[i] Shanghai Key Laboratory of Atmospheric Particle Pollution and Prevention (LAP³), Department of Environmental Science and Engineering, Fudan University, Shanghai, 200433, China

*Corresponding authors: Cheng Liu (chliu81@ustc.edu.cn); Keding Lu (k.lu@pku.edu.cn)

1 **ABSTRACT**
2 Ship based multi-axis differential optical absorption spectroscopy (MAX-DOAS) measurements were carried out
3 along the marginal seas of China from 19 April to 16 May 2018, to measures the vertical profiles of aerosol, NO₂ and
4 HONO. Five hot spots of tropospheric NO₂ VCDs were found in Yangtze River Delta, Taiwan straits,
5 Guangzhou-Hong Kong-Macao Greater Bay areas, Zhanjiang Port, and Qingdao port with averaged NO₂ VCDs of
6 1.07×10^{16}, 1.30×10^{16}, 7.27×10^{15}, 5.34×10^{15}, and 3.12×10^{15} molec. cm⁻², respectively. HONO performs similar
7 spatial distribution characteristics as NO₂ with averaged HONO VCDs in above five hot-spot areas of 1.01×10^{15},
8 7.91×10^{14}, 6.02×10^{14}, 5.36×10^{14}, and 5.17×10^{14} molec. cm⁻², respectively. The averaged near-surface NO₂
9 concentrations were 8.46 and 11.31 ppb, and the averaged near-surface HONO concentrations were 0.23 and 0.27 ppb
10 under viewing sea and viewing land observation azimuths during the whole campaign, respectively. The Chinese
11 Academy of Meteorological Sciences (CAMS) and Southern University of Science and Technology (SUST)
12 MAX-DOAS stations were selected as inland and coastal cases to further understand the impacts of relative humidity
13 (RH), temperature, and solar radiation intensity (SRI) on the heterogeneous reaction of NO₂ to form HONO in
14 different scenes. The emission ratios of $\Delta HONO/\Delta NO_x$ in sea, CAMS and SUST were 0.46±0.31%, 0.82±
15 0.34%, and 0.79±0.31%, respectively. The RH turning points in CAMS and SUST cases were all ~65% (60-70%),
16 however, two turning peaks (~60% and ~85%) of RH were found in sea cases. The HONO/NO₂ decrease along with
17 the increase of temperature, and with peak values on ~12.5℃ in CAMS. The HONO/NO₂ increase along with
18 increasing temperature, and with peak values on ~31.5℃ in SUST. In sea case, the HONO/NO₂ increase along with
19 the increase of temperature with a peak value on ~25.0℃ under the temperature being larger than 18.0℃. That means
20 the high temperature could contribute to the secondary formation of HONO in sea atmosphere. The correlation
21 analysis between HONO and aerosol in near-surface layer illustrated the ground surface plays a more important role
22 than aerosol surface during the HONO formation process from the heterogeneous reaction of NO₂ under inland case,
23 however, aerosol surface plays a more important role during above process under coastal and sea cases. Moreover, we
24 found the HONO generation rate from NO₂ heterogeneous reaction in sea case is larger than that in inland case in
25 higher atmospheric layers above 600 m.

26 **1 Introduction**

27 Nitrous acid (HONO) is an important part of the atmospheric nitrogen cycle, and plays a significant role in
28 atmospheric oxidation capacity (Alicke et al., 2003; Kleffmann et al., 2005). Previous studies reported the

29 contribution of HONO photolysis to OH radicals can reach 40-60%, and even more than 80% especially in the early
30 morning (Michoud et al., 2012; Ryan et al., 2018; Xue et al., 2020). OH radicals are one of the most important
31 oxidants in the atmosphere. They can oxidize and destroy most atmospheric pollutants, such as CO, NO_x (NO+NO_2),
32 SO_2 and volatile organic compounds (VOCs), thereby further promoting the formation of secondary pollutants (ozone
33 (O_3), peroxyacetyl nitrate (PAN), and secondary aerosols, etc.), leading to serious haze pollution events (Huang et al.,
34 2014). In addition, as a nitrosating agent, HONO can produce carcinogenic nitrite amines to threat to human health
35 (Zhang et al., 2015). Therefore, a full understanding of the source and formation mechanism of HONO has very
36 important scientific significance for the study of tropospheric oxidation and the control of secondary pollution.

37 At present, the known sources of HONO mainly include direct emissions from vehicles, ships, biomass burning and
38 soil, the homogeneous reaction of NO and OH radicals, the heterogeneous reaction of NO_2 on aerosols, vegetation,
39 ground and other types of surfaces, and the photolysis of nitrate particles (NO_3^-) (Wang et al., 2015). There are also
40 some obvious unknown HONO sources (Fu et al., 2019). The heterogeneous reaction of NO_2 as a source of HONO
41 has received continuous attention in recent years. It has been found that the heterogeneous reaction of NO_2 is one of
42 the most important sources of HONO in a variety of scenarios such as inland, coastal cities and offshore seas. Liu et al.
43 (2021) reported the contribution of heterogeneous reaction of NO_2 on aerosol surface to HONO is 19.2% in summer,
44 and this contribution of heterogeneous reaction of NO_2 on aerosol and ground surfaces to HONO can reach 54.6% in
45 winter in Beijing. Yang et al. (2021) and Zha et al. (2014) found that the generation rate of HONO through the
46 heterogeneous reaction of NO_2 under sea-wind conditions could elevate 3-4 times than that under land-wind
47 conditions in the northern coastal city of Qingdao and the southern coastal city of Hong Kong, respectively. Cui et al.
48 (2019) illustrated that the heterogeneous reaction of NO_2 on aerosol and sea surfaces is an important source of HONO
49 in East China Sea in summer. The process of HONO formed from the heterogeneous reaction of NO_2 is affected by
50 various atmospheric parameters. The relative humidity (RH), temperature, solar radiation intensity (SRI), aerosol
51 concentration and its relative surface area are the particularly important parameters. Previous works always use the
52 linear regression relationship between HONO/NO_2 and above parameters to characterize the influence of these
53 parameters on the formation of HONO through the heterogeneous reaction of NO_2. Wen et al. (2019) found that the
54 increased temperature could promote the heterogeneous reaction of NO_2 to form HONO in sea conditions. The
55 generation rate of HONO could increase rapidly, when the temperature is greater than 20 ℃. Gil et al. (2019) found
56 that the HONO formed from the heterogeneous reaction of NO_2 will increase along with the increase of RH when RH
57 is less than 80% in a case of land park using deep learning forced by measurement results. Fu et al. (2019) reported
58 that RH and SRI are the main parameters driving the heterogeneous reaction of NO_2 to form HONO in Pearl River
59 Delta, and it contributes 72% of the total source of HONO. Cui et al. (2019) found that the potential of heterogeneous
60 reaction of NO_2 to form HONO will increase with the increase of particle concentration and the specific surface area
61 of single particle in coastal cities.

62 However, previous researches generally focuses on the near-surface layer of a single scene, and attentions on the
63 influence mechanism of the heterogeneous reaction of NO_2 to form HONO in vertical direction and in different sea
64 and land scenes are insufficient, which limits the comprehensive assessment to understand the sea-land differences
65 and impact mechanism of HONO formed from the heterogeneous reaction of NO_2. NO_2 could be transported from
66 inland and coastal cities to offshore seas (Tan et al., 2018). This part of NO_2 can promote the HONO formation
67 through heterogeneous reaction on the high-level aerosol and sea surfaces in the atmosphere of sea (Zhang et al.,
68 2020). The formed HONO is completely likely to be transported to land cities at night under favorable weather
69 conditions. It will affect the atmospheric oxidation and air quality, and even endanger human health. In addition, the
70 vertical distributions and values of atmospheric meteorology and aerosol parameters are significantly different in land
71 and sea scenes, which provide different conditions for the heterogeneous reaction of NO_2 to form HONO in different
72 height layers. Moreover, aerosols and NO_2 have complex evolution and transmission characteristics in vertical
73 direction. The vertical upward transport of aerosol and NO_2 can promote the HONO formation through heterogeneous
74 reaction at high altitude, and the vertical downward transport of HONO will impact the atmospheric environment near
75 the ground. The vertical observations in land-sea scenes is also helpful to distinguish the contribution of the
76 heterogeneous reaction of NO_2 on the aerosol and ground/sea surfaces (Zhang et al., 2020).

77 At present, a variety of HONO measurement techniques have been developed, which can be roughly divided into wet
78 chemical methods, spectroscopy methods, and mass spectrometry methods, in principle (Cheng et al., 2013; Bernard
79 et al., 2016; Gil et al., 2019; Guo et al., 2020; Jordan et al., 2020). However, these technical methods can only
80 measure the HONO information near the surface layer. Zhang et al. (2020) measured the vertical distribution of
81 HONO by placing wet chemical HONO samplers at different heights of tower in Being during spring, and found the
82 maximum value of HONO appeared at 120 m sourced from the heterogeneous reaction of NO_2 on aerosol surface
83 under haze conditions. Meng et al. (2020) also used tower by moving the IBBCEAS carried in a box at a constant
84 speed to measure the vertical profiles of HONO in Beijing during winter, and reported that the heterogeneous reaction
85 of NO_2 under the atmospheric boundary layer is an important source of HONO, especially in haze conditions.
86 However, the cost of above techniques used to measure HONO vertical profiles is too high, and the real-time and
87 continuous measurement cannot be realized. Multi-axis differential optical absorption spectroscopy (MAX-DOAS), as

88 a ground-based ultra-hyperspectral remote sensing technology, has been widely used for vertical observation of
89 atmospheric pollutants in the past two decades. Therefore, the measurement of the vertical profiles of HONO under
90 different sea-land scenes based on MAX-DOAS could provide technical supports for learning the sea-land and
91 vertical differences and the influence mechanism of the heterogeneous reaction of NO_2 to form HONO. In the past
92 five years, several researchers have carried out campaigns based on MAX-DOAS to measure the vertical profile of
93 HONO in inland and coastal areas, and revealed the sources of HONO and their contribution to atmospheric oxidation
94 at different height layers (Garcia-Nieto et al., 2018; Wang et al., 2019). There are few studies on the sources of
95 HONO at different height layers in sea scene. In this study, it will be the first time to use MAX-DOAS to study the
96 spatiotemporal distribution and the sources of HONO along the Chinese coastline, and to learn the differences of the
97 HONO formed from the heterogeneous reaction of NO_2 in different height layers and land-sea scenes.

2 Methods and methodologies

2.1 The measurement cruise

100 The ship-based atmospheric observation campaign along the marginal seas of China was carried out from 19 April to
101 16 May 2018. The latitude and longitude ranges of the entire campaign covered 21.12°N-35.89°N and
102 110.67°E-122.16°E. The detailed voyage records of the observation ship are shown in Table 1. An integrated and fully
103 automated MAX-DOAS instrument was installed aboard the stern deck of the ship (Fig. S1(a)). In order to ensure that
104 the instrument is always kept in a horizontal position, a photoelectric gyro was used. The angle between the
105 observation direction and the heading direction of the ship was always maintained at 135° during the whole campaign.
106 The telescope unit of the instrument pointed towards sea during cruise NO.3 and NO.6. The telescope unit pointed
107 towards inland during cruise NO.1, NO.4 and NO.5. During cruise NO.2, the observation telescope always pointed to
108 Chongming island. The measurement ship only sailed in daytime from 19 April to 02 May, and continuously sailed in
109 all the daytime and nighttime from 3 May to 16 May 2018. The ship docked in Daishan port on 9-10 May and no
110 observations were carried out during these two days.

111 The aim of this campaign was to learn the vertical differences of NO_2 heterogeneous reaction to produce HONO in
112 marginal seas of China and compare the influence mechanism of that in inland cities. This study will provide
113 scientific guidance for understanding regional oxidation capacity and controlling the secondary air pollution.

2.2 MAX-DOAS measurements

2.2.1 Instrument setup

116 The compact instrument consists of an ultraviolet spectrometer (AvaSpec-ULS2048L-USB2, 300-460 nm spectral
117 range, 0.6 nm spectral resolution) at a 20℃ fixed temperature with a deviation of < 0.01℃, a one-dimensional CCD
118 detector (Sony ILX511, 2048 individual pixels) and a telescope unit driven by a stepper motor to collect scattered
119 sunlight from different elevation angles. The accuracy of elevation angle is < 0.1 ℃ and the telescope field of view
120 (open angle) is < 0.3°. A full scanning sequence consists of 11 elevation angles (1°, 2°, 3°, 4°, 5°, 6°, 8°, 10°, 15°, 30°
121 and 90°). The integration time of one individual spectrum was set to 30 s, and each scanning sequence took about 5.5
122 min. Besides, the controlling electronic devices and connecting fiber are mounted inside. The instrument is equipped
123 with a high-precision Global Position System (GPS) to record the real-time coordinated positions of the ship cruise.

2.2.2 Data processing and filtering

125 The MAX-DOAS measurements could be influenced by the exhaust from the measurement ship. Therefore, the data
126 contaminated by the exhaust were filtered out. As shown in Fig. S1(b), the direction and speed of the plume exhausted
127 from the ship depends on the ship direction/speed and the true wind speed/direction. Individual measurements taken
128 under unfavorable plume directions (plume directions between 45 and 135° with respect to the heading of the ship)
129 were discarded. In order to avoid the strong influence of the stratospheric absorption, the spectra measured with solar
130 zenith angle (SZA) lager than 75 ° were filtered out. Under these two filtering criteria, 4.9 and 8.3% of all data were
131 rejected before DOAS analysis (Xing et al., 2017, 2019, 2020).

2.2.3 DOAS analysis

133 The MAX-DOAS measured spectra were analyzed using the software QDOAS which is developed by BIRA-IASB
134 (http://uv-vis aeronomie.be/software/QDOAS/). The DOAS fit results are the differential slant column densities
135 (DSCDs), i.e. the difference of the slant column density (SCD) between the off-zenith spectrum and the
136 corresponding zenith reference spectrum. Details of the DOAS fit settings are listed in Table1. A typical DOAS
137 retrieval example for the oxygen dimer (O_4), nitrogen dioxide (NO_2) and nitrous acid (HONO) are shown in Fig. 1.
138 The stratospheric contribution was approximately eliminated by taking the zenith spectra of each scan as reference in
139 the DOAS analysis. Before profile retrieval, DOAS fit results of O_4, NO_2 and HONO with root mean square (RMS) of
140 residuals larger than 3×10^{-3} were filtered. Moreover, the SCD data under the color index (CI) being < 10% of the
141 thresholds obtained through fitting a fifth-order polynomial to CI data which is a function of time was filtered out, in
142 order to ensure a high signal-to-noise ratio (SNR) of the spectra. This filtering criteria remove 2.1, 3.9 and 5.3% for
143 O_4, NO_2 and HONO, respectively.

2.3 Vertical profile retrieval

Aerosol and trace gases (i.e., NO_2 and HONO) vertical profiles are retrieved from MAX-DOAS measurements using the algorithm reported by Liu et al. (2021). The inversion algorithm is developed based on the Optical Estimation Method (OEM) (Rodgers, 2000), which employs the radiative transfer model VLIDORT as the forward model. In this study, an exponential decreasing a priori with a scale height of 1.0 km was used as the initial profile for both the aerosol and trace gases retrieval. The surface concentrations of aerosol and trace gases were set to 0.3 km^{-1} and 5.0 ppb, respectively. We assume a fix set of aerosol optical properties with asymmetry parameter of 0.69, a single scattering albedo of 0.90 and ground albedo of 0.05. Moreover, the uncertainty of the aerosol and trace gases a priori profile was set to 100% and the correlation length was set to 0.5 km.

2.4 Ancillary data

Meteorological data (including temperature, pressure, relative humidity, visibility, solar radiation intensity, wind speed and wind direction) with a temporal resolution of 1 min was measured in the weather station installed on the ship. NO was measured using NO analyzer (Thermo Scientific model 42i) with a 1 min time resolution. The speed of the ship was calculated referred to the GPS data.

3 Results and Discussion

3.1 Overview of the MAX-DOAS observation over marginal seas of China

A radiative transfer model SCIATRAN was used to convert SCDs of NO_2 and HONO to their tropospheric vertical column densities (VCDs). The vertical profiles of aerosol, NO_2 and HONO retrieved from MAX-DOAS, the temperature and pressure vertical profiles simulated using a dynamical-chemical model (WRF-Chem), and the geo-position data collected by GPS were introduced as inputs in SCIATRAN for the NO_2 and HONO air mass factor (AMF) calculation. Missing data are due to power and instrument system failure, interference of ship plume, unfavorable weather condition (i. e., heavy rain), and night sailing. During the cruise of Chongming to Zhanjiang, NO_2 VCDs varied from 1.05×10^{14} to 4.02×10^{16} molec.cm^{-2} with an averaged value of 3.90×10^{15} molec. cm^{-2}. NO_2 VCDs varied from 1.08×10^{14} to 2.60×10^{16} molec.cm^{-2} with an averaged value of 4.27×10^{15} molec. cm^{-2} from Zhanjiang to Qingdao. From Chongming to Zhanjiang, HONO VCDs varied from 1.00×10^{14} to 2.58×10^{15} molec. cm^{-2} with a mean value of 2.39×10^{14} molec. cm^{-2}. From Zhanjiang to Qingdao, HONO VCDs varied from 1.01×10^{14} to 2.61×10^{15} molec. cm^{-2} with a mean value of 2.74×10^{14} molec. cm^{-2}.

Figure 2 showed the spatial distribution of NO_2 and HONO VCDs over the marginal seas of China. It should be noted that five elevated tropospheric NO_2 VCDs hot spots were observed during the whole campaign, i.e., the coastal areas of Yangtze River Delta, Taiwan straits, Guangzhou-Hong Kong-Macao Greater Bay areas, Zhanjiang Port, and Qingdao port. In the coastal areas of Yangtze River Delta, the hot spots were mainly distributed in the Yangtze River estuary, Hangzhou Bay, Ningbo port, Taizhou port, and Wenzhou port. These areas are mostly important shipping channels or shipping ports, and are great NO_2 emission sources. The averaged NO_2 VCDs in above five areas reached 1.07×10^{16}, 1.30×10^{16}, 7.27×10^{15}, 5.34×10^{15}, and 3.12×10^{15} molec. cm^{-2}, respectively. HONO exhibited similar spatial distribution characteristics as NO_2, and the averaged HONO VCDs in above five hot-spot areas reached 1.01×10^{15}, 7.91×10^{14}, 6.02×10^{14}, 5.36×10^{14}, and 5.17×10^{14} molec. cm^{-2}, respectively. It indicates that NO_2 is an important precursor of HONO. Previous studies have reported that HONO can produced from NO_2 through heterogeneous reaction on the surface of aerosol and sea (Yang et al., 2021). However, there are obvious differences in the concentration distribution of HONO and NO_2 in the southeast coastal area of Jiangsu (from Qidong to Dongtai). In this area, NO_2 showed a higher concentration (1.66×10^{16} molec. cm^{-2}, 4 times higher than the mean NO_2 VCD), while HONO showed a lower concentration (2.06×10^{14} molec. cm^{-2}, ~80% of the mean HONO VCD). It might be the fresh ship emission plume on the route enhancing the NO_2 concentration and HONO has not been fully formed from NO_2 heterogeneous reaction in time, due to the observations from ship-based MAX-DOAS are instantaneous. On the other hand, the solar radiation intensity in this day (12 May, 2018) was significantly lower than other days (Fig. S2), and this weather condition was not conductive to the HONO formation through the heterogeneous reaction of NO_2.

The surface concentration of NO_2 and HONO were extracted from their corresponding vertical profiles. As shown in Figure 3, the total averaged near-surface NO_2 concentrations under viewing sea and viewing land conditions were 8.46 and 11.31 ppb, respectively. The total averaged near-surface HONO concentrations were 0.23 and 0.27 ppb under viewing sea and viewing land conditions. Previous studies reported that vehicle and ship emissions were the main HONO primary sources on land and sea, respectively, and NO_2 heterogeneous reaction on the surfaces of ground, sea, vegetation and aerosol were the HONO important secondary sources (Liu et al., 2021). They also found the surface HONO concentration under sea case was lower than that under land case, especially in the morning and evening (Yang et al., 2021). Figure 4 shows the time series of AOD, the surface concentrations of NO_2 and HONO, and the surface HONO/NO_2 during the whole campaign. We could find the time series of AOD and NO_2 are similar. The high AOD and NO_2 usually appeared in busy shipping channels and ports, and the obvious high-value areas are the coast of the Yangtze River Delta, the Taiwan Strait, Xiamen port, Zhanjiang port and Qingdao port (with a 1.28 mean AOD and a 18.90 ppb mean NO_2). HONO always appeared under high AOD and NO_2 conditions, however,

202 high AOD and NO₂ were not necessarily accompanied with high production rate of HONO. This is because the
203 heterogeneous formation of HONO requires suitable meteorological conditions (i.e., RH and temperature) in addition
204 to its precursor (NO₂) and the reaction surface (aerosol) (Liu et al., 2019). The high HONO/NO₂ values were found on
205 02, 13 and 14 May with an average value of 0.45 during the whole campaign. Moreover, we found the high values of
206 HONO/NO₂ always appeared from 11:00 to 14:00 during a whole day. That is due to the high production rate of
207 HONO and the high photolysis rate of NO₂ during noontime.

3.2 The relationship between HONO/NO₂ with RH, Temperature and aerosol in land and sea

209 In order to fully understand the differences of the impacts of RH, temperature and aerosol on the HONO secondary
210 formation in land and sea conditions, the Chinese Academy of Meteorological Sciences (CAMS) and Southern
211 University of Science and Technology (SUST) MAX-DOAS stations were selected as inland and coastal areas for
212 analysis, respectively. Sun et al. (2020) reported that HONO concentrations could increase up to 40–100% over the
213 navigation areas, and Huang et al. (2017) reported vehicle exhaust could contribute to ~12-49% of the atmospheric
214 HONO budget. Since the direct emissions of the measurement ship have been removed before data analysis, the
215 primary source of HONO during the whole campaign was mainly from the direct emissions of cargo ships. We used
216 an averaged $0.46 \pm 0.31\%$ emission ratio of $\Delta HONO / \Delta NO_x$ in this study referring to Sun et al. (2020) to understand
217 the primary source of HONO on the sea surface during the campaign. The NO was measured using in situ instrument,
218 and sea-surface NO₂ was extracted from the retrieved NO₂ vertical profiles (NO$_x$ = NO + NO₂). In addition, the
219 calculation method of emission ratios of $\Delta HONO / \Delta NO_x$ in CAMS and SUST was referred to Xu et al. (2015) and
220 Xing et al. (2021). The averaged emission ratios in CAMS and SUST were $0.82 \pm 0.34\%$ and $0.79 \pm 0.31\%$,
221 respectively. The direct emissions have been deduced in the following study of the secondary formation of HONO.
222 Moreover, the secondary formation pathway of HONO are believed mainly from the heterogeneous reaction of NO₂
223 on the surface. The linear regression between HONO and NO₂ in land and static sea scenarios is shown in Figure 5.
224 We found the fitting slopes in static sea scenes was ~8-10 times larger than that in land scenes, especially on the static
225 condition viewing sea (slope $\approx$ 0.06). The correlation coefficients (R) in inland and static sea scenes were all > 0.62,
226 except in SUST (R = 0.58). That indicates the formation rate of secondary HONO from NO₂ heterogeneous reaction
227 in static sea scenes might be faster than that in land scenes.

3.2.1 RH dependence on HONO formation

229 The scatter plots of HONO/NO₂ against RH in different land and sea conditions are illustrated in Figure 6. In order to
230 eliminate the influence of other factors, the average of six highest HONO/NO₂ in each 10% RH interval is calculated.
231 We found the RH turning points in inland (CAMS) and coastal (SUST) cases are all ~65% (60-70%). The
232 HONO/NO₂ increases along with RH when RH is less than 65%, and the HONO/NO₂ will decrease when RH is larger
233 than 65%. That means it contributes to the HONO formation from the heterogeneous reaction of NO₂ on wet surfaces
234 with the gradual increase of RH until 65%. The decrease of HONO/NO₂ with RH larger than 65% is presumably due
235 to the efficient uptake of HONO on wet surfaces and the wet surfaces being less accessible or less reactive to NO₂
236 when RH being larger than 65% (Liu et al., 2019). However, two turning peaks of RH were found in sea cases. The
237 first RH turning peak occurred in ~60%, which is the similar with that under inland and coastal cases. While another
238 RH turning peak appeared in ~85% (80-90%). That means high RH also could increase the HONO formation in sea
239 cases. In addition, the HONO/NO₂ decreased sharply when RH was larger than 95%, because the reaction surface will
240 asymptotically approach a water droplet state to limit the formation of HONO with RH larger than 95%.

3.2.2 Temperature dependence on HONO formation

242 The scatter plots of HONO/NO₂ against temperature in different land and sea conditions are shown in Figure 7. To
243 eliminate the influence of other factors, the average of the six highest HONO/NO₂ values in each 5℃ temperature
244 interval is calculated. In inland condition (CAMS), the HONO/NO₂ decrease along with the increase of temperature,
245 and the HONO/NO₂ peak values appeared on the temperature being ~12.5℃. However, we found the HONO/NO₂
246 increase along with increasing temperature, and the peak values of HONO/NO₂ appeared with ~31.5℃ temperature
247 in coastal condition (SUST). That indicates the HONO formation from NO₂ heterogeneous reaction will be
248 accelerated under lower and higher temperature in inland and coastal conditions, respectively. In sea condition, the
249 HONO/NO₂ increase along with the increase of temperature with a peak value under ~25.0℃ temperature when the
250 atmospheric temperature was larger than 18.0℃, simultaneously, a ~1.9 averaged HONO/NO₂ high value was found
251 under ~15.0℃ (14.0-17.0℃) temperature. Moreover, we found that the appearance of HONO/NO₂ peak values under
252 lower temperature (14.0-17.0℃) usually accompanied by landing wind. Wen et al. (2019) also reported that relatively
253 high temperature could contribute to the formation of HONO in sea condition.

3.2.3 Impact of aerosol on HONO formation

255 In order to further understand the HONO formation from NO₂ heterogeneous reaction on aerosol surface, several
256 correlation analyses were carried out. As shown in Figure 8, the linear regression plots between HONO and aerosol,

257 and between HONO/NO$_2$ and aerosol in land and sea conditions were performed. It was found that the correlation
258 coefficient (R) between HONO and aerosol varied in the order of coastal (0.55) > sea (0.51) > inland (0.14). In
259 addition, the fitting slopes under coastal and sea conditions (0.07) are about 2.3 times larger than that under inland
260 condition (0.03). That means the ground surface maybe more important than aerosol surface during the process of
261 HONO formed from NO$_2$ heterogeneous reaction in the ground surface layer of inland. In coastal and sea conditions,
262 the aerosol and sea are all important to provide heterogeneous reaction surface for NO$_2$ to form HONO (Cui et al.,
263 2019; Wen et al., 2019; Yang et al., 2021). In addition, we found the averaged values of HONO/NO$_2$ are 0.011, 0.014
264 and 0.008 when aerosol extinctions are 0-0.3, 0.3-0.6, and 0.6-0.9 km^{-1} in inland case, respectively. The high values of
265 HONO/NO$_2$ are mainly under aerosol extinction being less than 1.0 km^{-1} with averaged values of 0.16 and 0.32 in
266 coastal and sea cases, respectively. It indicates that aerosol surface plays a more important role to form HONO
267 through NO$_2$ heterogeneous reaction in sea condition than that in land condition.

268 **3.3 Vertical distributions of HONO/NO$_2$ under different aerosol condition in land and sea**

269 In order to further investigate the height dependence of HONO/NO$_2$ under land and sea conditions, two cases in Pearl
270 River Delta (PRD) were selected from the whole campaign. As shown in Figure 9, "A" and "B" were under similar
271 aerosol level (the extinction coefficients in surface layer being 0.45-0.60 km^{-1}) and vertical distribution structure, and
272 were all observed from 10:00 to 11:00. The instrument viewed sea accompanied with sea wind in "A" named sea
273 scene, and the instrument viewed land accompanied with land wind in "B" named land scene. The NO$_2$ in sea and
274 land scenes have a similar vertical structure, and the NO$_2$ concentration in land scene are larger than that in sea scene
275 except on the surface layer. The HONO have the same vertical distribution structure in above two scenes, and the
276 HONO concentration in land scene always larger than that in sea scene. In Figure 9(e), we found that HONO/NO$_2$
277 under 0-400 m in land scene is higher than that in sea scene, however, the HONO/NO$_2$ values are obviously lower in
278 land scene than that in sea scene above 400 m. Moreover, the growth rate of HONO/NO$_2$ with the increase of height
279 in sea scene is significantly faster than that in land scene above 400 m. It indicates the generation rates of HONO
280 sourced from NO$_2$ heterogeneous reaction on aerosol surface in sea scene is larger than that in land scene above 400
281 m. Under 400 m, the HONO generation rates in land scene is larger than that in sea scene.

282 In addition, we selected inland cases (CAMS) to learn the difference of height dependence of HONO/NO$_2$ compared
283 with scenes. As shown in Figure 10, the sea and inland scenes have the similar aerosol levels (low aerosol level: < 0.2
284 km^{-1}) and vertical structure. Moreover, the NO$_2$ and HONO in sea and inland scenes have the similar vertical structure,
285 but their concentrations in sea scene are all larger than that in inland scene. In Figure 10(d), we could find the
286 HONO/NO$_2$ in sea scene is obviously larger than that in inland scene above 400 m. The HONO/NO$_2$ in sea scene is
287 about 4.5 times larger than that in inland scene especially above 600 m. As shown in Figure 11, the aerosols under sea
288 and inland scenes are also with the similar extinction levels (relatively high level: ~0.8 km^{-1}) and vertical structure.
289 The NO$_2$ concentration in sea scene is higher than that in inland scene with a similar vertical structure. The HONO
290 concentration in sea scene is lower than that in inland scene under 400 m, while it in sea scene is larger than that in
291 inland scene above 400 m. In Figure 11 (d), we found the HONO/NO$_2$ in inland scene is larger than that in sea scene
292 under 600 m, while the HONO/NO$_2$ in sea scene is about 2 times larger than that in inland scene above 600 m. Above
293 all cases indicate that the HONO generation rate from NO$_2$ heterogeneous reaction in sea scene is larger than that in
294 inland scene in higher atmospheric layers above 400-600 m. The high-altitude (> 400-600 m) atmospheric parameters
295 in sea scene are more conductive to promote the HONO formation through the heterogeneous reaction of NO$_2$.

296 **3.4 Case study**

297 **3.4.1 20 April: A typical transport event**

298 As shown in Figure 12, the aerosol mainly distributed in 0-200 m with a mean extinction coefficient larger than 0.74
299 km^{-1}. NO$_2$ was mainly distributed near the ground surface with a mean concentration 28.54 ppb before 13:20. The
300 NO$_2$ during this period might come from local ship emissions, due to this area is a main shipping channels. From
301 14:25 to 17:10, a high-concentration NO$_2$ air mass (averaged 13.29 ppb) was found at ~2.0 km. In order to understand
302 their source of this high-altitude NO$_2$ air mass, we further investigated the possible influence of transport by using the
303 backward trajectories. We calculated 24 h backward trajectories of air masses at 500, 1000 and 2000 m using
304 HYSPLIT (Hybrid Single-Particle Lagrangian Integrated Trajectory) developed by the National Oceanic and
305 Atmospheric Administration Air Resource Laboratory (NOAA-ARL). The meteorological data with a 1°×1° spatial
306 resolution and 24 layers were collected from the Global Data Assimilation System (GDAS). In Figure 13, we found
307 that the dominant wind direction during this period was southeast at all 500, 1000 and 2000 m. The transport of air
308 masses carried NO$_2$ emitted by ships in Ningbo and Zhoushan ports, to main cargo ports of China, to Shanghai.
309 Moreover, the concentration of NO$_2$ was low (averaged 2.32 ppb) near the ground surface from 14:25 to 17:10. As
310 shown in Figure 12 (e) and (g), a low pressure (< 1020 hPa), north dominant wind direction with the wind speed > 12
311 m/s appeared at ground surface during this period. That means the clean air from north reduced the local surface NO$_2$.
312 The HONO was mainly distributed near the surface with a mean concentration of 0.07 ppb, and two peaks were found
313 at the early morning (averaged 0.15 ppb) and 12:15 (averaged 0.11 ppb), respectively. The relatively high
314 concentration of HONO appeared in the early morning was accumulated with the stabilization of boundary layer and

315 attenuation of solar radiation after the sunset the day before (Xing et al., 2021). The HONO peak appeared at 12:15
316 might source from the heterogeneous reaction of NO_2 on the aerosol surface under a ~80% RH, a 18.5℃ temperature,
317 and a 1×10^3 W/m^2 SRI conditions.

3.4.2 28 April: A typical event of HONO produced from NO_2 heterogeneous reaction

319 The measurement ship moored at Xiamen port on 28 April. This is a typical port observation case. As shown in Figure
320 14, we found there are two peaks for aerosol and NO_2 at 09:00-11:00 and 14:00-16:00 (averaged aerosol extinction
321 coefficient > 0.8 km^{-1}, averaged NO_2 concentration > 12.0 ppb), respectively. NO_2 was mainly distributed near the sea
322 surface layer 0-200 m, and there was a high-concentration NO_2 air mass being found in 1.0-2.0 km during
323 13:00-14:00 due to the short distance transport of NO_2 emitted from ships in Xiamen port. However, aerosol appeared
324 in the range of 0.0-2.0 km during 09:00-11:00 and 14:00-16:00. In Figure 14 (g), we found the wind speeds in above
325 two peak periods were obviously higher than other periods. In 09:00-11:00, the wind speed was ~5.0 m/s with a
326 northwest dominant direction (urban), and the wind speed was ~6.0 m/s with a southeast dominant direction (port
327 gateway) during 14:00-16:00. That indicates the short-distance high-altitude transport caused the appearance of
328 high-extinction aerosol mass during above two periods.

329 Moreover, we found the high-concentration HONO only appeared at 14:00-16:00 with a 0.57 ppb averaged
330 concentration under 0.9 km, while it was only about 0.14 ppb during 09:00-11:00 period. The higher RH and
331 temperature (Tem) (RH: ~75.0%, Tem: 23.7℃) at 14:00-16:00 than that (RH: ~67.6%, Tem: 23.1℃) at 09:00-11:00
332 (Figure 14 (d)-(e)) promoted the HONO formation from the heterogeneous reaction of NO_2 on the aerosol surface
333 during 14:00-16:00. On the other hand, the solar radiation intensity (SRI) (~600 W/m^2) at 09:00-11:00 was obviously
334 larger than that (~250 W/m^2) at 14:00-16:00 (Figure 14 (f)). The higher SRI accelerated the photolysis of HONO
335 during 09:00-11:00 period. Therefore, the lower formation rate and higher photolysis rate leaded to a significantly
336 lower HONO concentration at 09:00-11:00 that that at 14:00-16:00.

3.4.3 03 May: A typical event with unknown HONO source

338 The measurement ship carried out observation in the sea area near Zhanjiang on 03 May, 2018. As shown in Figure 15,
339 we found there was an obvious sinking process for aerosol from ~1.0 km during 09:00-16:00, and eventually
340 accumulated near the sea surface with a high extinction coefficient > 0.92 km^{-1}. The NO_2 was mainly concentrated
341 near the sea surface layer (0-400 m) with an averaged concentration of 8.93 ppb from 08:00 to 09:00. Afterwards,
342 with the rise the planetary boundary layer (PBL) height after sunrise, NO_2 was gradually mixed and spread throughout
343 the PBL from 09:00 to 13:00. During this period, it is accompanied by the increase of the NO_2 concentration
344 (averaged 11.2 ppb) under PBL. It is due to the contribution of ship emissions near the sea surface. On the other hand,
345 the regional transport of NO_2 from land also increased the NO_2 concentration in this sea area, with the wind speed
346 increase from 2.5 to 7.8 m/s with a north wind direction from 10:00 to 16:00 (Figure 15 (g)).

347 Several HONO peaks (> 0.2 ppb) at 0.5-1.0 km were found from 10:00 to 13:00, and the aerosol and NO_2 high values
348 were also observed at this height layer, simultaneously. That means the heterogeneous reaction of NO_2 on aerosol
349 surface is more important than that on the sea surface for HONO source under sea atmosphere. In addition, HONO
350 concentration obviously elevated after 14:00, especially during 14:00-16:00 (> 0.4 ppb). It might source from
351 heterogeneous reaction of NO_2 on the aerosol surface, under RH a being ~92.5% (Figure 15 (d)). The photolysis of
352 HONO also decreased with SRI < 150 W/m^2 (Figure 15 (f)) during this period. Moreover, a HONO peak (> 0.32 ppb)
353 was observed during 16:40-17:10. However, the NO_2 always kept lower concentration (< 1.5 ppb) after 16:00, the
354 temperature was lower than 17 ℃ (Figure 15 (e)), and it indicates the heterogeneous reaction of NO_2 being not the
355 source of this HONO peak. The wind was north dominant with an average speed at 7.8 m/s after 15:00, and it means
356 the regional transport might not be the source of this high-concentration HONO. Moreover, the SRI was lower than
357 87.5 W/m^2, and it shows the photolysis of nitrate aerosol also being not the source of the elevated HONO. The
358 unknown HONO source in this sea area need to be further explored.

4 Summary and Conclusions

360 Ship based MAX-DOAS observations along the marginal seas of China were performed from 19 April to 16 May
361 2018, simultaneously, two ground based MAX-DOAS observations were carried out in the inland station CAMS and
362 the coastal station SUST during the same time to measure the aerosol, NO_2, and HONO vertical profiles to learn the
363 sea-land and vertical differences of NO_2 heterogeneous reaction to produce HONO. The latitude and longitude ranges
364 of the entire ship based campaign covered 21.12ºN-35.89ºN and 110.67ºE-122.16ºE, respectively. We found five hot
365 spots of tropospheric NO_2 and HONO VCDs in Yangtze River Delta, Taiwan straits, Guangzhou-Hong Kong-Macao
366 Greater Bay areas, Zhanjiang Port, and Qingdao port. The averaged values of NO_2 in above five areas were $1.07\times$
367 10^{16}, 1.30×10^{16}, 7.27×10^{15}, 5.34×10^{15}, and 3.12×10^{15} molec. cm^{-2}, and the averaged HONO concentrations in
368 above five areas were 1.01×10^{15}, 7.91×10^{14}, 6.02×10^{14}, 5.36×10^{14}, and 5.17×10^{14} molec. cm^{-2}, respectively.
369 However, we found NO_2 showed a higher concentration (1.66×10^{16} molec. cm^{-2}), while HONO showed a lower
370 concentration (2.06×10^{14} molec. cm^{-2}) in the southeast coastline of Jiangsu province. Moreover, the averaged

near-surface NO_2 concentrations were 8.46 and 11.31 ppb, and the averaged near-surface HONO concentrations were 0.23 and 0.27 ppb under viewing sea and viewing land observation azimuths during the whole campaign, respectively. HONO always appeared under high AOD and NO_2 conditions.

In order to further understand the impacts of RH, temperature, and SRI on the heterogeneous reaction of NO_2 to produce HONO, the emission rates of $\Delta HONO / \Delta NO_x$ in sea, inland and coastal areas were calculated with values of $0.46\pm0.31\%$, $0.82\pm0.34\%$, and $0.79\pm0.31\%$ to remove the primary HONO source. We found the RH turning points in CAMS and SUST are all ~65% (60-70%). The HONO/NO_2 increased with increase of RH under 65%, and the HONO/NO_2 decreased when RH is larger than 65%. However, two turning peaks (~60% and ~85%) of RH were found in sea case. That means high RH could contribute to the secondary formation of HONO in sea atmosphere. Moreover, the HONO/NO_2 decreased with the increase of temperature, and with peak values on ~12.5℃ in CAMS, however, it increase with increasing temperature, and peaked at ~31.5℃ in SUST. In sea case, the HONO/NO_2 increased with the increase of temperature with a peak value on ~25.0℃ under the temperature > 18.0℃, simultaneously, a ~1.9 averaged HONO/NO_2 high value was found under ~15.0℃. It illustrated the high temperature could promote the formation of HONO from NO_2 heterogeneous reaction in sea and coastal atmosphere. In addition, the correlation analysis under different sea-land conditions told us the ground surface plays a more important role than aerosol surface during the HONO formation from the heterogeneous reaction of NO_2 under inland case, while the aerosol surface plays a more important role during above process under coastal and sea cases. Furthermore, we found that the HONO/NO_2 in sea case is about 4.5 times larger than that in inland case above 600 m under aerosol extinction coefficient ~0.2 km^{-1}, and the HONO/NO_2 in sea case is about 2 times larger than that in inland case above 600 m under aerosol extinction coefficient ~0.8 km^{-1}. That means the generation rate of HONO from NO_2 heterogeneous reaction in sea case is larger than that in inland CASE in higher atmospheric layers above 600 m.

Acknowledgements

This research is supported by the National Natural Science Foundation of China (42207113, U21A2027), the Anhui Provincial Natural Science Foundation (2108085QD180), the Presidential Foundation of the Hefei Institutes of Physical Science, Chinese Academy Sciences (YZJJ2021QN06), the National Natural Science Foundation of China (51778596, 41575021 and 41977184), the Strategic Priority Research Program of the Chinese Academy of Sciences (XDA23020301), the National High-Resolution Earth Observation Project of China (No. 05-Y30B01-9001-19/20-3). We would like to also thank Fudan University (Professor Jianmin Chen's group) for organizing the ship-based campaign and providing meteorological data.

Compliance with ethics guidelines

All authors (the name of author) declare that they have no conflict of interest or financial conflicts to disclose.

References

[1] Alicke B, Geyer A, Hofzumahaus A, et al. OH formation by HONO photolysis during the BERLIOZ experiment, J. Geophys. Res.-Atmos., 2003, 108, 8247.

[2] Kleffmann J, Gavriloaiei T, Hofzumahaus A, et al. Daytime formation of nitrous acid: A major source of OH radicals in a forest, Geophys. Res. Lett., 2005, 32, L05818.

[3] Michoud V, Kukui A, Camredon M, et al. Radical budget analysis in a suburban European site during the MEGAPOLI summer field campaign. Atmos. Chem. Phys., 2012, 12, 11951–11974.

[4] Ryan RG, Rhodes S, Tully M, et al. Daytime HONO, NO_2 and aerosol distributions from MAX-DOAS observations in Melbourne. Atmos. Chem. Phys., 2018, 18, 13969–13985.

[5] Xue C, Zhang C, Ye C, et al. HONO Budget and Its Role in Nitrate Formation in the Rural North China Plain. Environ. Sci. Technol., 2020, 54, 11048-11057.

[6] Huang R, Zhang Y, Bozzetti C, et al. High secondary aerosol contribution to particulate pollution during haze events in China. Nature, 2014, 514, 218-222.

[7] Zhang B, Wang Y, Hao J. Simulating aerosol-radiation-cloud feedbacks on meteorology and air quality over eastern China under severe haze conditions in winter. Atmos. Chem. Phys., 2015, 15, 2387–2404.

[8] Wang L, Wen L, Xu C, et al. HONO and its potential source particulate nitrite at an urban site in North China during the cold season. Sci. Total Environ., 2015, 538, 93–101.

[9] Fu X, Wang T, Zhang L, et al. The significant contribution of HONO to secondary pollutants during a severe winter pollution event in southern China. Atmos. Chem. Phys., 2019, 19, 1–14.

[10] Liu J, Liu Z, Ma Z, et al. Detailed budget analysis of HONO in Beijing, China: Implication on atmosphere oxidation capacity in polluted megacity. Atmos. Environ., 2021, 244, 117957.

[11] Yang Y, Li X, Zu K, et al. Elucidating the effect of HONO on O_3 pollution by a case study in southwest China. Sci. Total Environ., 2021, 756, 144127.

[12] Zha Q, Xue L, Wang T, et al. Large conversion rates of NO_2 to HNO_2 observed in air masses from the South China Sea: Evidence of strong production at sea surface? Geophys. Res. Lett., 2014, 41, 7710–7715.

[13] Cui L, Li R, Fu H, et al. Formation features of nitrous acid in the offshore area of the East China Sea. Sci. Total Environ., 2019, 682, 138–150.

[14] Wen L, Chen T, Zheng P, et al. Nitrous acid in marine boundary layer over eastern Bohai Sea, China: Characteristics, sources, and implications. Sci. Total Environ., 2019, 670, 282–291.

[15] Gil G, Kim J, Lee M, et al. The role of HONO in O_3 formation and insight into its formation mechanism during the KORUS-AQ Campaign. Atmos. Chem. Phys. Discus., 2019, https://doi.org/10.5194/acp-2019-1012.

[16] Cui L, Li R, Zhang Y, et al. An observational study of nitrous acid (HONO) in Shanghai, China: The aerosol impact on HONO formation during the haze episodes. Sci. Total Environ., 2018, 630, 1057–1070.

[17] Tan W, Liu C, Wang S, et al. Tropospheric NO_2, SO_2, and HCHO over the East China Sea, using ship-based MAX-DOAS observations and comparison with OMI and OMPS satellite data. Atmos. Chem. Phys., 2018, 18, 15387–15402.

[18] Zhang W, Tong S, Jia C, et al. Different HONO Sources for Three Layers at the Urban Area of Beijing. Environ. Sci. Technol., 2020, 54, 12870-12880.

[19] Cheng P, Cheng Y, Lu K, et al. An online monitoring system for atmospheric nitrous acid (HONO) based on stripping coil and ion chromatography. J. Environ. Sci., 2013, 25(5) 895–907.

[20] Bernard F, Cazaunau M, Grosselin B, et al. Measurements of nitrous acid (HONO) in urban area of Shanghai, China. Environ. Sci. Pollut. Res., 2016, 23:5818–5829.

[21] Jordan N, Osthoff HD. Quantification of nitrous acid (HONO) and nitrogen dioxide (NO_2) in ambient air by broadband cavity-enhanced absorption spectroscopy (IBBCEAS) between 361 and 388 nm. Atmos. Meas. Tech., 2020, 13, 273–285.

[22] Guo Y, Wang S, Gao S, et al. Influence of ship direct emission on HONO sources in channel environment. Atmos. Environ., 2020, 242, 117819.

[23] Meng F, Qin M, Tang K, et al. High-resolution vertical distribution and sources of HONO and NO_2 in the nocturnal boundary layer in urban Beijing, China. Atmos. Chem. Phys., 2020, 20, 5071–5092.

[24] Garcia-Nieto D, Benavent N, Saiz-Lopez A. Measurements of atmospheric HONO vertical distribution and temporal evolution in Madrid (Spain) using the MAX-DOAS technique. Sci. Total Environ., 2018, 643, 957–966.

[25] Wang Y, Dörner S, Donner S, et al. Vertical profiles of NO_2, SO_2, HONO, HCHO, CHOCHO and aerosols derived from MAX-DOAS measurements at a rural site in the central western North China Plain and their relation to emission sources and effects of regional transport. Atmos. Chem. Phys., 2019, 19, 5417–5449.

[26] Xing C, Liu C, Wang S, et al. Observations of the vertical distributions of summertime atmospheric pollutants and the corresponding ozone production in Shanghai, China. Atmos. Chem. Phys. 2017, 17, 14275–14289.

[27] Xing C, Li C, Wang S, et al. A new method to determine the aerosol optical properties from multiple-wavelength O_4 absorptions by MAX-DOAS observation. Atmos. Meas. Tech., 2019, 12, 3289–3302.

[28] Xing C, Liu C, Wang S, et al. Identifying the wintertime sources of volatile organic compounds (VOCs) from MAX-DOAS measured formaldehyde and glyoxal in Chongqing, southwest China. Sci. Total Environ., 2020, 715, 136258.

[29] Vandaele AC, Hermans C, Simon PC, et al. Measurements of the NO_2 absorption cross-section from 42,000 cm^{-1} to 10,000 cm^{-1} (238–1000 nm) at 220K and 294 K. J. Quant. Spectrosc. Ra., 1998, 59, 171–184.

[30] Serdyuchenko A, Gorshelev V, Weber M, et al. High spectral resolution ozone absorption cross-sections –part 2: temperature dependence. Atmos. Meas. Tech., 2014, 7, 625–636.

[31] Thalman R, Volkamer R. Temperature dependent absorption cross-sections of O_2–O_2 collision pairs between 340 and 630 nm and at atmospherically relevant pressure. Phys. Chem. Chem. Phys., 2013, 15, 15371–15381.

[32] Meller R, Moortgat GK. Temperature dependence of the absorption cross sections of formaldehyde between 223 and 323 K in the wavelength range 225–375 nm. J. Geophys. Res., 2000, 105, 7089–7101.

[33] Rothman L, Gordon I, Barber R, et al. HITEMP, the high-temperature molecular spectroscopic database. J. Quant. Spectrosc. Ra., 2010, 111, 2139–2150.

[34] Fleischmann OC, Hartmann M, Burrows JP, et al. New ultraviolet absorption cross-sections of BrO at atmospheric temperatures measured by time-windowing Fourier transform spectroscopy. J. Photoch. Photobio., 2004, A 168, 117–132.

[35] Stutz J, Kim ES, Platt U, et al. UV–visible absorption cross sections of nitrous acid. J. Geophys. Res.-Atmos., 2000, 105, 14585–14592.

[36] Aliwell S, Van Roozendael M, Johnston P, et al. Analysis for BrO in zenith-sky spectra: an Intercomparison exercise for analysis improvement. J. Geophys. Res., 2002, 107, 4199.

[37] Liu C, Xing C, Hu Q, et al. Ground-based hyperspectral stereoscopic remote sensing network: A promising strategy to learn coordinated control of O_3 and $PM_{2.5}$ over China. Engineering, 2021.

[38] Liu Y, Nie W, Xu Z, et al. Semi-quantitative understanding of source contribution to nitrous acid (HONO) based on 1 year of continuous observation at the SORPES station in eastern China. Atmos. Chem. Phys., 2019, 19, 13289–13308.

[39] Sun L, Chen T, Jiang Y, et al. Ship emission of nitrous acid (HONO) and its impacts on the marine atmospheric oxidation chemistry. Sci. Total Environ., 2020, 735, 139355.

[40] Huang R, Yang L, Cao J, et al. Concentration and sources of atmospheric nitrous acid (HONO) at an urban site in Western China. Sci. Total Environ., 2017, 593–594, 165–172.

[41] Xu Z, Wang T, Wu J, et al. Nitrous acid (HONO) in a polluted subtropical atmosphere: Seasonal variability, direct vehicle emissions and heterogeneous production at ground surface, Atmos. Environ., 2015, 106, 100–109.

[42] Xing C, Liu C, Hu Q, et al. Vertical distributions of wintertime atmospheric nitrogenous compounds and the corresponding OH radicals production in Leshan, southwest China. J. Environ. Sci., 2021, 105, 44–55.

496 **Table 1. Detailed information of the measurement cruise**

Cruise NO.	Periods	Measurement cruise
NO. 1	08:50 to 21:02 19 Apr.	Daishan port (30.24ºN, 122.16ºE) to Chongming (31.18ºN, 121.82ºE)
NO. 2	05:40 to 17:45 20 Apr.	Sailing around Chongming island
NO. 3	06:03 21 Apr. to 08:07 03 May	Chongming (31.18ºN, 121.82ºE) to Zhanjiang port (21.12ºN, 110.67ºE)
NO. 4	08:07 03 May to 06:52 09 May	Zhanjiang port (21.12ºN, 110.67ºE) to Daishan port (30.24ºN, 122.16ºE)
NO. 5	05:40 11 May to 05:55 14 May	Daishan port (30.24ºN, 122.16ºE) to Qingdao (35.89ºN, 120.87ºE)
NO. 6	05:55 14 May to 10:00 16 May	Qingdao (35.89ºN, 120.87ºE) to Daishan port (30.24ºN, 122.16ºE)

497

498 **Table 2. Detailed retrieval settings of O_4, NO_2 and HONO.**

Parameter	Data source	Fitting internals (nm)		
		O_4	NO_2	HONO
Wavelength range		338-370	338-370	335-373
NO_2	298K, I_0-corrected, Vandaele et al. (1998)	√	√	√
NO_2	220K, I_0-corrected, Vandaele et al. (1998)	√	√	√
O_3	223K, I_0-corrected, Serdyuchenko et al. (2014)	√	√	√
O_3	243K, I_0-corrected, Serdyuchenko et al. (2014)	√	√	√
O_4	293K, Thalman and Volkamer (2013)	√	√	√
HCHO	298K, Meller and Moortgat (2013)	√	√	√
H_2O	HITEMP (Rothman et al. 2010)	×	×	√
BrO	223K, Fleischmann et al. (2004)	√	√	√
HONO	296K, Stutz et al. (2000)	×	×	√
Ring	Calculated with QDOAS	√	√	√
Polynomial degree		Order 5	Order 5	Order 5
Intensity offset		Constant	Constant	Constant

499 * Solar I_0 correction; Aliwell et al. (2002).

500
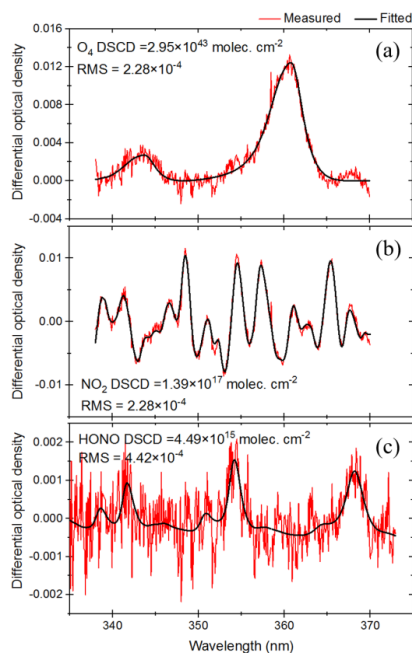
501

502 Figure 1. Typical DOAS spectral fittings for (a) O_4, (b) NO_2 and (c) HONO.

503
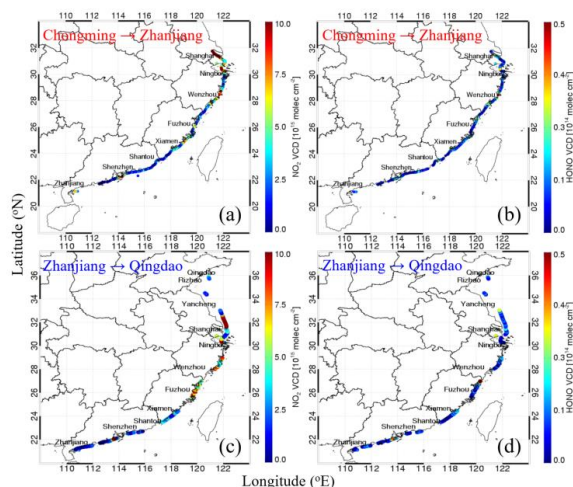
504

505   Figure 2. The spatial distributions of NO₂ and HONO VCDs. (a) and (b) show the NO₂ and HONO
506   VCDs along the cruise route from Chongming to Zhanjiang. (c) and (d) depict the NO₂ and HONO
507   VCDs along the cruise route from Zhanjiang to Qingdao.

508
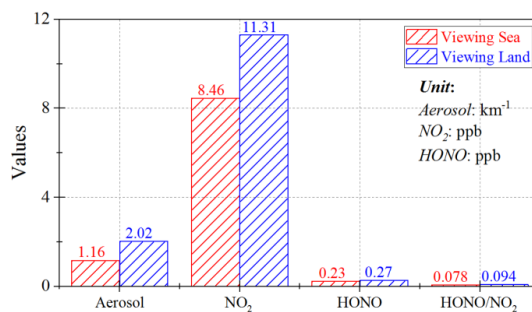
509

510   Figure 3. Averaged aerosol extinction, NO₂ concentration, HONO concentration and HONO/NO₂ ratio
511   on two viewing directions (Viewing sea: red; Viewing inland: blue) during the campaign.

512
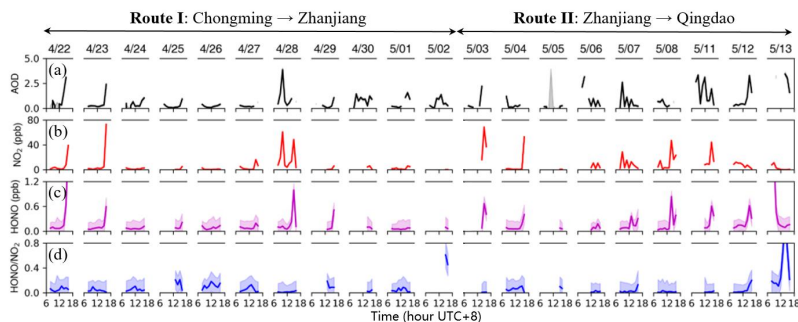
513

514   Figure 4. Time series of (a) AOD, (b) surface NO₂ concentration, (c) surface HONO concentration, and
515   (f) surface HONO/NO₂ ratios.

516

517
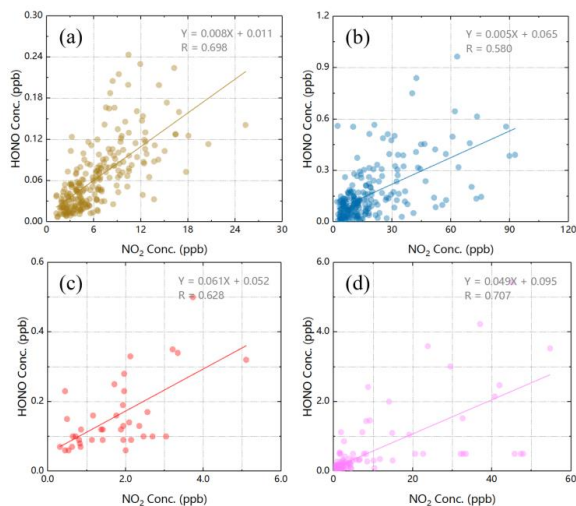
518   Figure 5. Linear regression plots of surface NO_2 and HONO concentrations in CAMS (a), SUST (b),
519   static condition viewing sea (c), and static condition viewing inland (d).

520

521
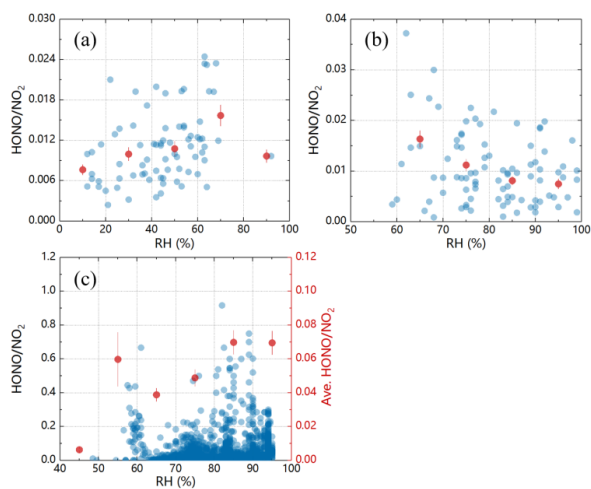
522   Figure 6. Scatter plots of RH and HONO/NO_2 ratios in (a) CAMS, (b) SUST, and (c) this ship-based
523   campaign.

524

525
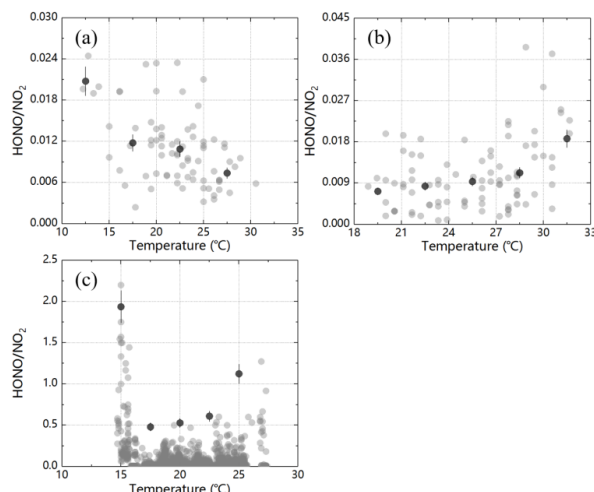
526   Figure 7. Scatter plots of temperature and HONO/NO$_2$ ratios in (a) CAMS, (b) SUST, and (c) this
527   ship-based campaign.

528

529
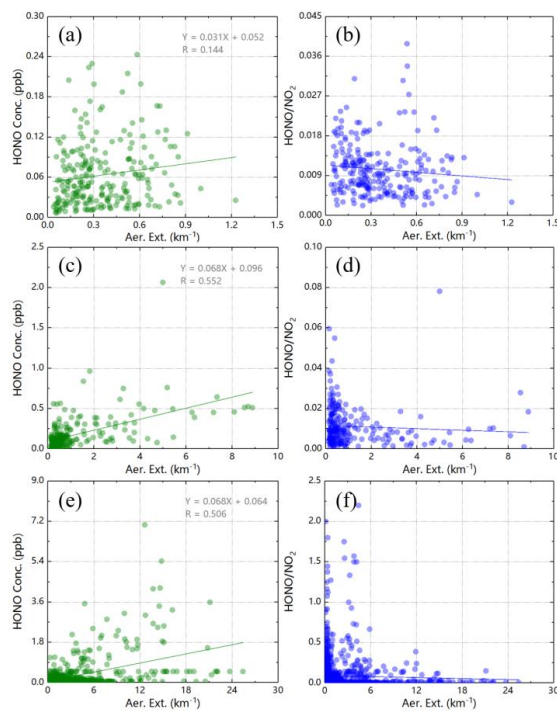
530   Figure 8. (a), (c) and (e) show the linear regression plots of surface aerosol extinction and HONO
531   concentrations in CAMS, SUST and this ship-based campaign, respectively. (b), (d) and (f) depict
532   the scatter plots of surface aerosol extinction and HONO/NO$_2$ ratios in CAMS, SUST and this
533   ship-based campaign.

534

535
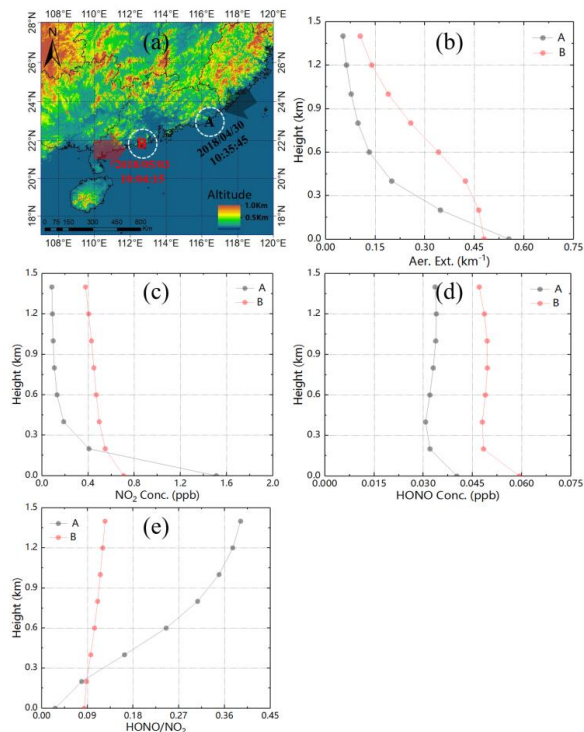
Figure 9. (a) shows two measurement points (A: black, viewing sea with sea wind; B: red, viewing
inland with inland wind) during the campaign. (b)-(e) show the vertical profiles of aerosol, NO_2,
HONO, and HONO/NO_2 ratios in above two measurement points, respectively.

539

540
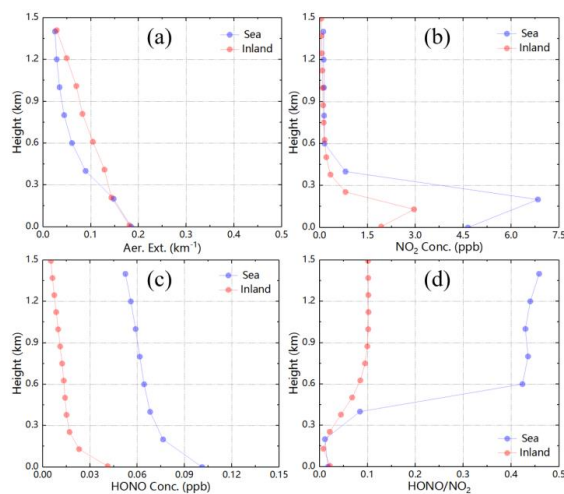
Figure 10. Vertical distributions of (a) aerosol extinction, (b) NO_2 concentration, (c) HONO
concentration, and (d) HONO/NO_2 ratio. The blue and red lines represent a ship-based campaign
case and a CAMS inland case, respectively.

544

545

546
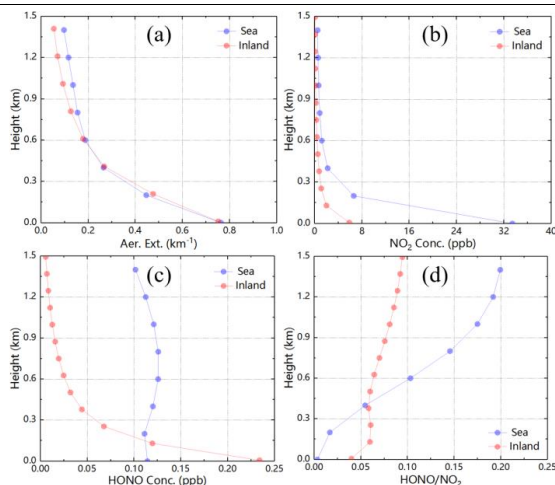
Figure 11. Vertical distributions of (a) aerosol extinction, (b) NO$_2$ concentration, (c) HONO
concentration, and (d) HONO/NO$_2$ ratio. The blue and red lines represent a ship-based campaign
case and a CAMS inland case, respectively.

550

551
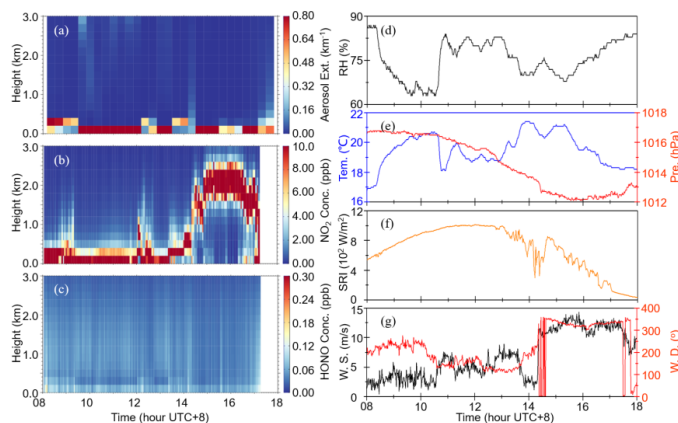
Figure 12. Case of 20 April 2018. Time series of (a) aerosol extinction, (b) NO$_2$ and (c) HONO vertical
profiles, respectively. (d) shows the time series of surface RH. (e) depicts the time series of surface
temperature and pressure. (f) shows the time series of surface SRI. (g) depicts the time series of
surface wind speed and wind direction.

556
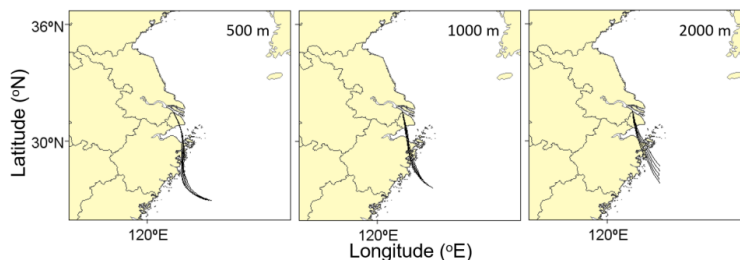
557

558   Figure 13. Daily 24 h backward trajectories of air masses at (a) 500 m, (b) 1000 m, and (c) 2000 m on
559   20 April 2018, respectively.

560
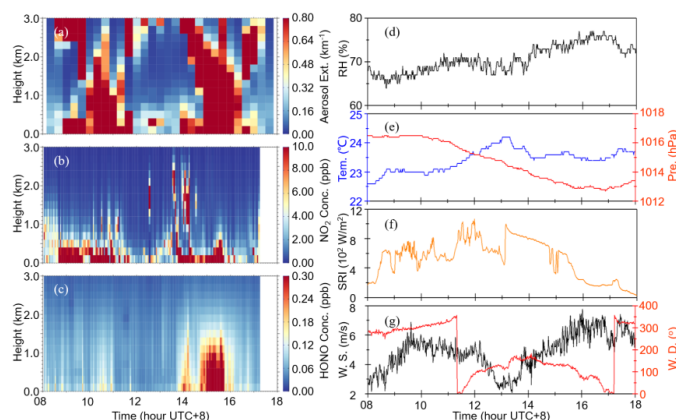
561

562   Figure 14. Case of 28 April 2018. Time series of (a) aerosol extinction, (b) NO₂ and (c) HONO vertical
563   profiles, respectively. (d) shows the time series of surface RH. (e) depicts the time series of surface
564   temperature and pressure. (f) shows the time series of surface SRI. (g) depicts the time series of
565   surface wind speed and wind direction.

566
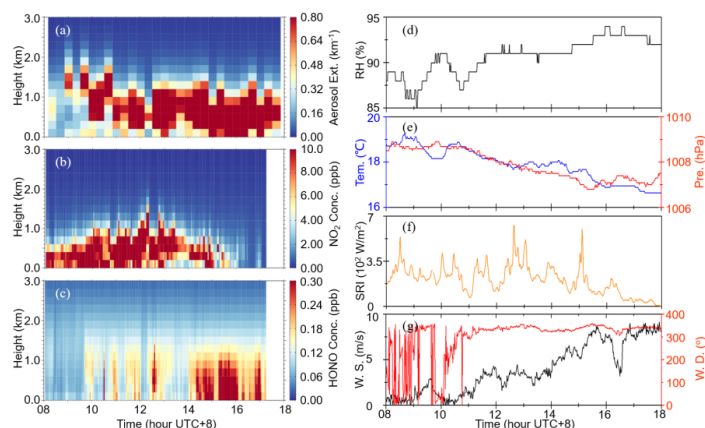
567

568   Figure 15. Case of 03 May 2018. Time series of (a) aerosol extinction, (b) NO₂ and (c) HONO vertical
569   profiles, respectively. (d) shows the time series of surface RH. (e) depicts the time series of surface
570   temperature and pressure. (f) shows the time series of surface SRI. (g) depicts the time series of
571   surface wind speed and wind direction.

572

573